

## Multidimensional Interface Topology Induced by Acoustic Wannier Configurations

Peng Zhang,<sup>1,2</sup> Han Jia<sup>2,3,\*</sup>, Jiuyang Lu,<sup>4,†</sup> Xinghang Yang,<sup>1,2</sup> Suhao Wang,<sup>1,2</sup> Xiangyuan Xu,<sup>1,2</sup> Yuzhen Yang<sup>2,3,‡</sup>, Zhengyou Liu,<sup>5,6,‡</sup> and Jun Yang<sup>1,2,§</sup>

<sup>1</sup>Key Laboratory of Noise and Vibration Research, Institute of Acoustics, Chinese Academy of Sciences, Beijing 100190, People's Republic of China


<sup>2</sup>University of Chinese Academy of Sciences, Beijing 100049, People's Republic of China

<sup>3</sup>State Key Laboratory of Acoustics, Institute of Acoustics, Chinese Academy of Sciences, Beijing 100190, People's Republic of China

<sup>4</sup>School of Physics and Optoelectronics, South China University of Technology, Guangzhou 510641, People's Republic of China

<sup>5</sup>Key Laboratory of Artificial Micro- and Nano-Structures of Ministry of Education and School of Physics and Technology, Wuhan University, Wuhan 440072, People's Republic of China

<sup>6</sup>Institute for Advanced Studies, Wuhan University, Wuhan 440072, People's Republic of China

 (Received 10 June 2022; revised 25 October 2022; accepted 16 November 2022; published 30 December 2022)

Recently, real-space representations, revealing in depth the duality of topological descriptions in real and momentum space, have been applied to show multidimensional crystalline topology. Here we propose nontrivial phononic crystals by constructing different Wannier configurations based on real-space representations. We experimentally achieve the symmetry-protected interface topology in multiple dimensions containing anomalous interface states and higher-order corner states. Nontrivial acoustic pseudospin polarizations are critical to the interface states and have been directly observed in experiment. In a consistent frame, the higher-order corner states arising from the fractional charge anomaly are further observed. Our study provides a scheme based on Wannier configurations for designing topological metamaterials, which is fruitful for characterizing and manipulating multidimensional topological states and can be generalized to other classical systems.

DOI: [10.1103/PhysRevApplied.18.064094](https://doi.org/10.1103/PhysRevApplied.18.064094)

### I. INTRODUCTION

Topological materials have been successfully categorized by symmetries that both determine the topological classification and protect the nontrivial boundary states [1–6]. Sparked by the real-space representations of crystalline symmetries [7,8], a systematic procedure of discovery and classification of topological crystals has been established [9–12]. At the core is the construction of the relations between the band topology in momentum space and the Wannier functions, which are the real-space counterparts of Bloch waves [13,14]. From the real-space representation viewpoint, topological crystals can be classified with respect to the spatial distributions of symmetric Wannier functions (SWFs) together with the carried charges, i.e., the Wannier configurations. The gapless boundary states in the first-order topological phases are also viewed

as obstructions to their Wannier configuration depictions [9]. Wannier configurations have more importance for the higher-order topological systems where intrinsic bulk multipole moments manifest lower-order boundary charges [15–18]. In addition to revealing the boundary signatures, Wannier configurations have been further extended to multidimensional systems hosting specific spatial symmetries to constitute genuine topological invariants [19–22]. To date, Wannier configurations have been utilized to characterize different types of topological systems, including eigenvalue fragile phases [22,23] and bulk-disclination correspondence [24].

Phononic crystals (PCs), by virtue of their flexible designability, have become a versatile wave-control platform to explore diverse band topology, such as one-way boundary transport [25–30], higher-order corner states [31–36], non-Abelian topological charges [37,38], and artificial gauge flux [39]. For these wave manipulations, acoustic waves are often characterized as scalar fields. Recently, key transport properties, denoted as the local angular momentum, are unveiled by fully considering the vectorial features of the acoustic waves [40–42]. In

\*hjia@mail.ioa.ac.cn

†phjylu@scut.edu.cn

‡zyliu@whu.edu.cn

§jyang@mail.ioa.ac.cn

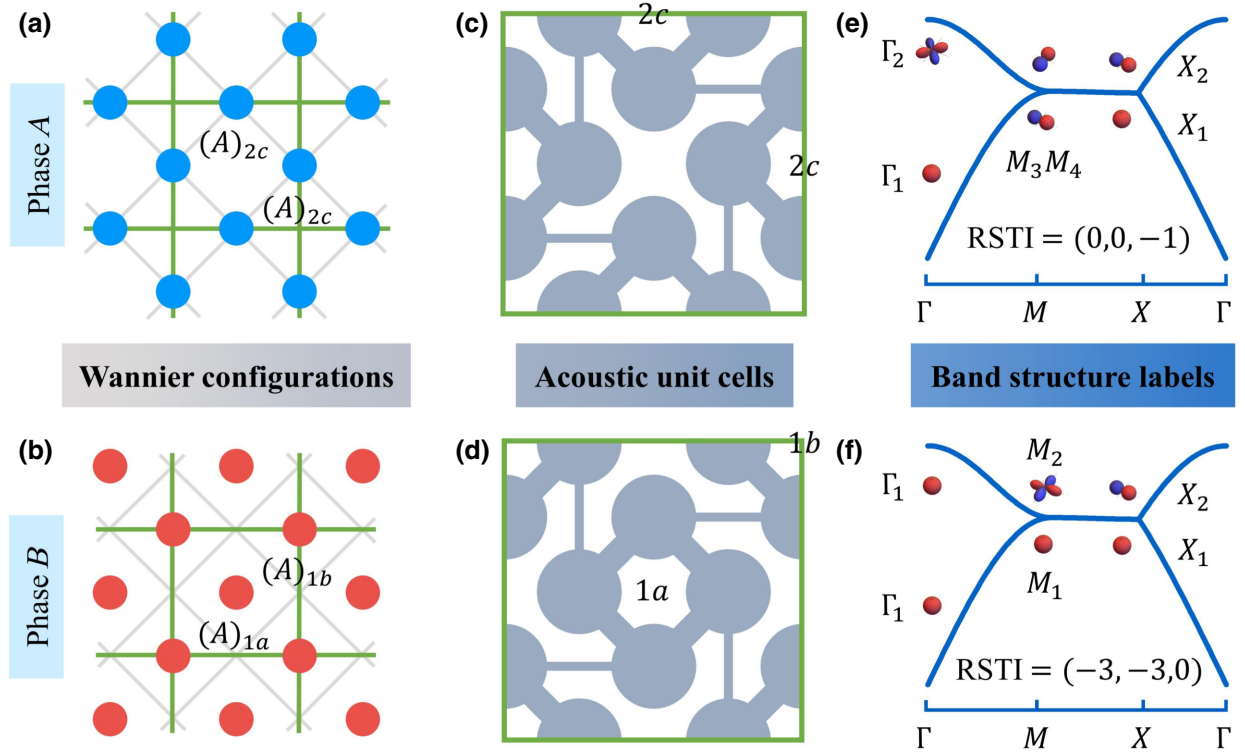


FIG. 1. Realizing acoustic topological bands via Wannier configurations. (a),(b) Schematic Wannier configurations in distinct topological phases. The SWFs localize at the WPs  $2c$  (blue) in phase  $A$  and at the WPs  $1a$  and  $1b$  (red) in phase  $B$ , corresponding to different EBRs. Gray and green squares denote the primitive and enlarged unit cells, respectively. (c),(d) Top views of designed PC structures of phases  $A$  and  $B$ . (e),(f) Simulated bands for PCs of phases  $A$  and  $B$ , respectively, with the labeled real-space topological indices. The orbitals at high-symmetry points represent schematically the corresponding acoustic fields.

practice, the local angular momentum can be expressed as the curl of Poynting vectors and is directly related to the acoustic velocity field, which has been introduced to emulate spin in acoustic systems [43,44] and to achieve spin-related acoustic wave manipulation [45–47]. However, the curl of Poynting vectors has yet to be utilized to experimentally characterize topological boundary states, and the effect of local angular momentum on acoustic topological transport has not been fully studied.

In this article, we propose a paradigm of designing topologically distinct PCs by constructing specific Wannier configurations in real space. Gapless interface states are constructed based on the spatial mismatch of SWFs. With direct measurements of acoustic Poynting vectors, the first-order topological interface transports are experimentally characterized by acoustic pseudospins. Furthermore, we experimentally realize the higher-order corner states arising from the mismatch between the local corner charges and the fourfold ( $C_4$ ) rotation symmetry of the PCs.

## II. UNIT CELLS WITH DIFFERENT WANNIER CONFIGURATIONS

Real-space positions in a unit cell can be categorized into a few Wyckoff positions (WPs) with respect to their

site symmetry groups [19]. For a square lattice with fourfold ( $C_4$ ) rotation symmetry, the WPs are the center ( $1a$ ), the corner ( $1b$ ), and the midpoint of the edge ( $2c$ ), as labeled in Figs. 1(a) and 1(b). Focusing on the first band in a primitive cell (grey squares), the SWF can localize at either  $1a$  or  $1b$ . However, by doubling the primitive cell, we obtain an enlarged unit cell (green squares) where two types of the SWF locations are supported: one is the WPs  $1a$  and  $1b$ ; the other is the WP  $2c$ . Two different Wannier configurations are thus constructed and identified as phases  $A$  and  $B$ , with respect to the inherited SWF distributions. Specifically, the SWFs of phase  $A$  center at the WP  $2c$  [Fig. 1(a), blue circles]. For phase  $B$ , they are at both  $1a$  and  $1b$  [Fig. 1(b), red circles]. These SWFs induce corresponding elementary band representations (EBRs)  $(A)_{1a}$ ,  $(A)_{1b}$ , and  $(A)_{2c}$  [9,22], where  $A$  denotes the irreducible representations and the subscripts indicate the WPs. With these EBRs, the corresponding band structures can be labeled and topologically classified as discussed in the following.

According to the SWF distributions, we design two PCs for phases  $A$  and  $B$ , with their structures shown in Figs. 1(c) and 1(d), respectively. The PCs are based on the Shastry-Sutherland model [48] in the absence of magnetic fields, where the sites and hoppings correspond to cavities and connecting (thick and thin) tubes. The PCs of phases  $A$

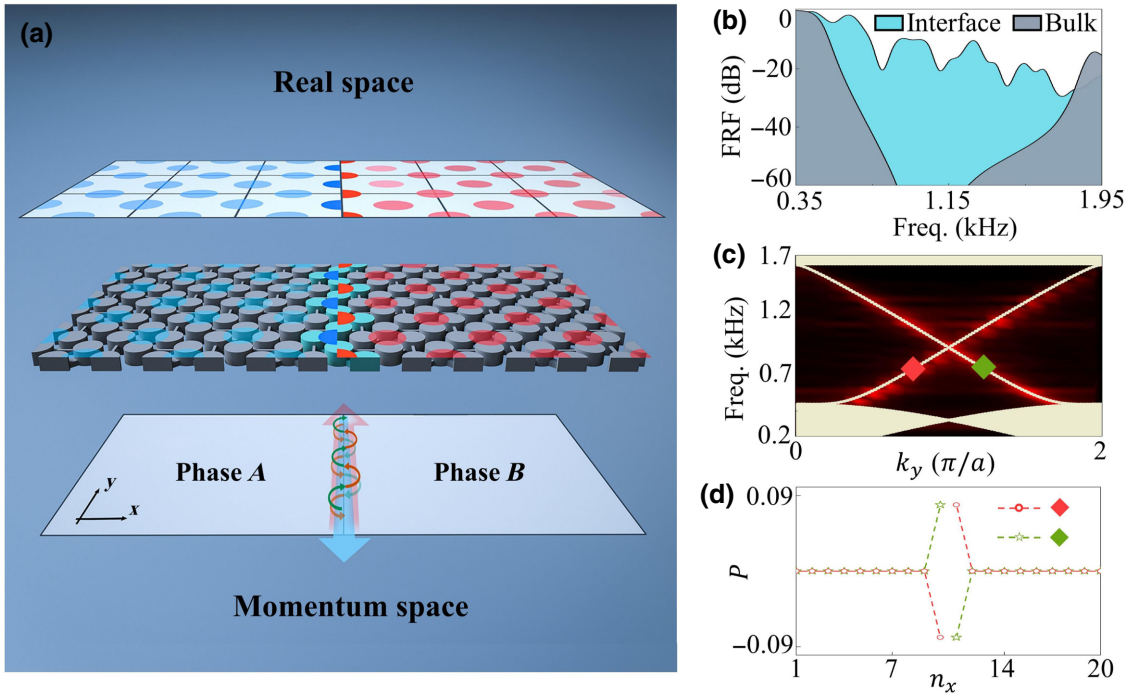


FIG. 2. (a) Illustrations for Wannier configurations and the corresponding interface states. The real-space Wannier configurations (upper panel) are attached to the domain wall constructed by PCs in different phases (middle panel), giving rise to the interface states hosting PP locking features (lower panel). (b) Measured FRFs for the interface and bulk states. (c) Simulated (yellow shapes) and measured (background color map) projected dispersions. (d) Simulated PP distributions of the interface states corresponding to the wave vectors  $k_y = 0.8$  and  $1.2$  in units of  $\pi/a$  [red and green dots in (c)];  $n_x$  is unit cell number.

and  $B$  share identical geometrical parameters (see Sec. 1 in Ref. [49]). Every four cavities linked by the thick tubes form a single plaquette, and the thin tubes connecting the plaquettes break the mirror symmetries along the  $x$  and  $y$  directions, giving rise to the symmetries of group  $p4$ . The plaquettes are terminated at the boundaries to emulate the boundary located Wannier functions. For phases  $A$  and  $B$ , the acoustic fields mainly reside in the plaquettes at the WPs  $2c$  and WPs  $1a$  and  $1b$ , respectively. Compatible with the lattice symmetry, the fields in the plaquettes are linearly combined to construct the allowed orbitals in group  $p4$ , i.e., the SWFs within certain EBRs. For the designed PCs of phases  $A$  and  $B$ , the first two bands are numerically simulated as shown in Figs. 1(e) and 1(f), respectively; see Appendix A for simulation details. Although these two phases have identical band structures, they are depicted, according to the EBR theory, by different sets of symmetry labels at high-symmetry points. Schematic eigenstates are plotted with the simulated band structures, together showing the acoustic SWFs required in momentum space. The complete simulations of bands and the acoustic pressure profiles of the eigenstates are in Sec. 2 of Ref. [49].

The topology underpinning the two phases is expressed by the real-space topological indices (RSTIs). By constructing a one-to-one correspondence between band structures and real-space Wannier functions, a set of linear

equations is obtained for solving these RSTIs. The results generally contain ten integer components since the SWFs can be classified into ten types with respect to their WPs and symmetries, as tabulated in Appendix B. However, the RSTIs can be reduced to a triplet  $(\nu_{1a,1}, \nu_{1b,1}, \nu_{2c,1})$  due to the restriction that only monopole states survive at the  $\Gamma$  point for the first acoustic band. The subscripts in the RSTIs denote the WPs and representation indicators of the SWFs. The calculated RSTIs are  $(0, 0, -1)$  for phase  $A$  and are  $(-3, -3, 0)$  for phase  $B$  (Appendix B). These reduced RSTIs point towards different localized SWFs and directly pinpoint phases  $A$  and  $B$  with distinct crystalline topology.

### III. SNAKING INTERFACE STATES INDUCED BY WANNIER CONFIGURATIONS

With phases  $A$  and  $B$ , we construct the snaking interface states based on the spatial mismatch of the two Wannier configurations described previously. We construct the proposed interface states by combining the phases  $A$  and  $B$  in a way that retains the glide symmetry  $\mathcal{G}_y := (x, y) \rightarrow (-x, y + a/2)$  along the  $y$  direction, and the obtained interface is illustrated in the middle panel of Fig. 2(a). We measure the frequency-resolved response functions (FRFs) and provide the results in Fig. 2(b). The interface states ranging from 0.55 to 1.85 kHz are reflected by a much

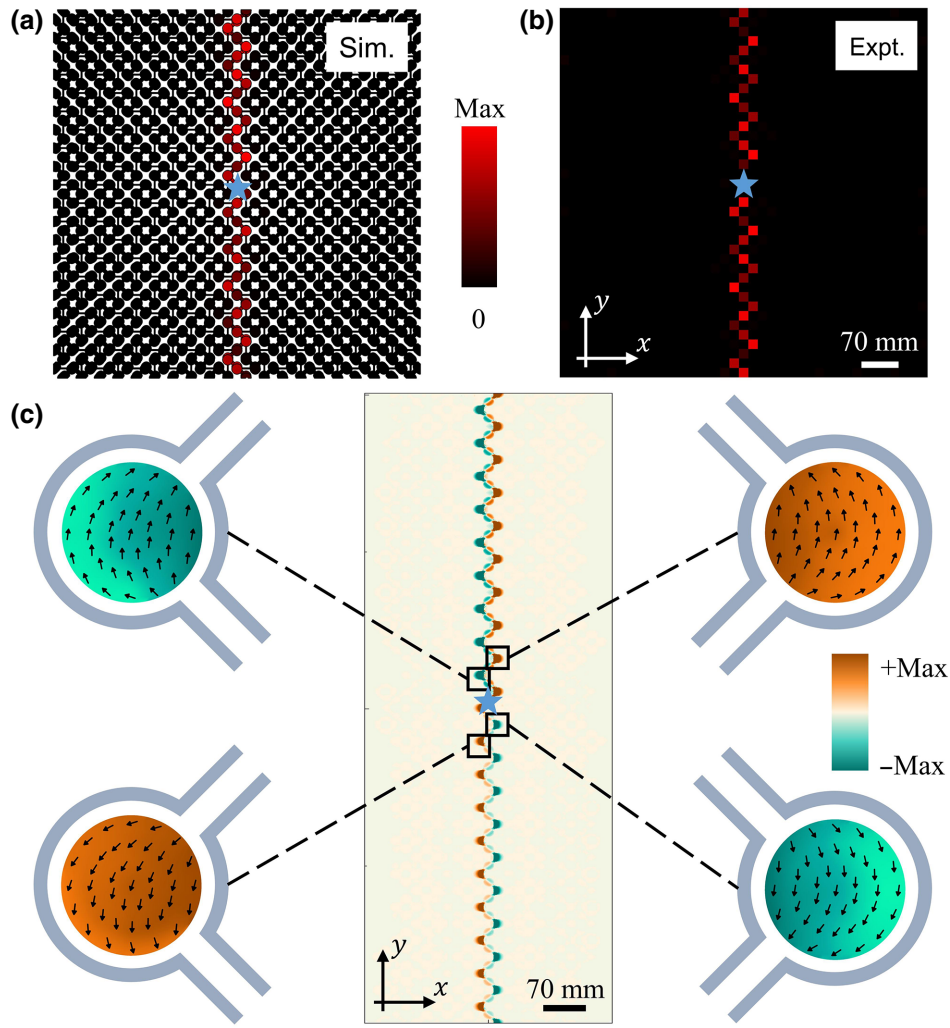


FIG. 3. Acoustic pressure fields and PP distributions of the interface states. (a),(b) Simulated and measured acoustic pressure amplitude profiles of the interface states at the frequency of 1.4 kHz. The blue stars denote excitation sources. (c) PP distributions of the interface. Middle panel is the simulation result of the  $z$  component of the curl of Poynting vectors. Four insets show the measured acoustic Poynting vectors with normalization in unit cells, where the arrows with normalized length show acoustic Poynting vector fields and the color maps denote the  $z$  components of the curl of the measurements.

higher interface FRF than that of the bulk one with a maximum value of over 40 dB. In Fig. 2(c), we provide the simulated (lines) and measured (color map) dispersions of interface states. These results coincide well and show that two interface bands traverse the ultrawide band gap and connect the bulk bands. The measurement details are in Appendix A.

It should be emphasized that our snaking interface state cannot be predicted by traditional Wilson loop calculations for either phase  $A$  or phase  $B$  (see Appendix C). Instead, the gapless feature of the interface states is protected by the SWF distributions on the interface between phases  $A$  and  $B$ , which can be revealed by the Wannier configurations shown in the upper panel of Fig. 2(a). On the interface, the SWFs localized at the WPs  $2c$  (red) and  $1b$  (blue) render the fractional charges  $1/2$  and  $1/4$ , respectively. The

SWF in the bulk renders charge 1 and makes no contribution to the interface. Hence, the SWFs contributing to the interface states are linear combinations of the SWFs  $2c$  in phase  $A$  and  $1b$  in phase  $B$ , and delocalize along the interface when the band gap stays closed. Namely, the associated Wannier centers can be located at any position along the line connecting the two WPs ( $2c$  and  $1b$ ) [9] and flows along the interface, giving rise to the gapless interface states.

Furthermore, we attach acoustic pseudospin polarizations (PPs) for a certain momentum to the unit cells, and demonstrate the nontrivial interface transport properties of snaking through the PCs of both phases. The PP for each unit cell is defined as  $P = \iint (\nabla \times \mathcal{S}_{\text{ave}})_z dx dy$ , where  $\mathcal{S}_{\text{ave}} = \text{Re}((1/2)p^* \mathbf{v})$  is the time-averaged Poynting vector for acoustic waves and the integration is over one unit cell.

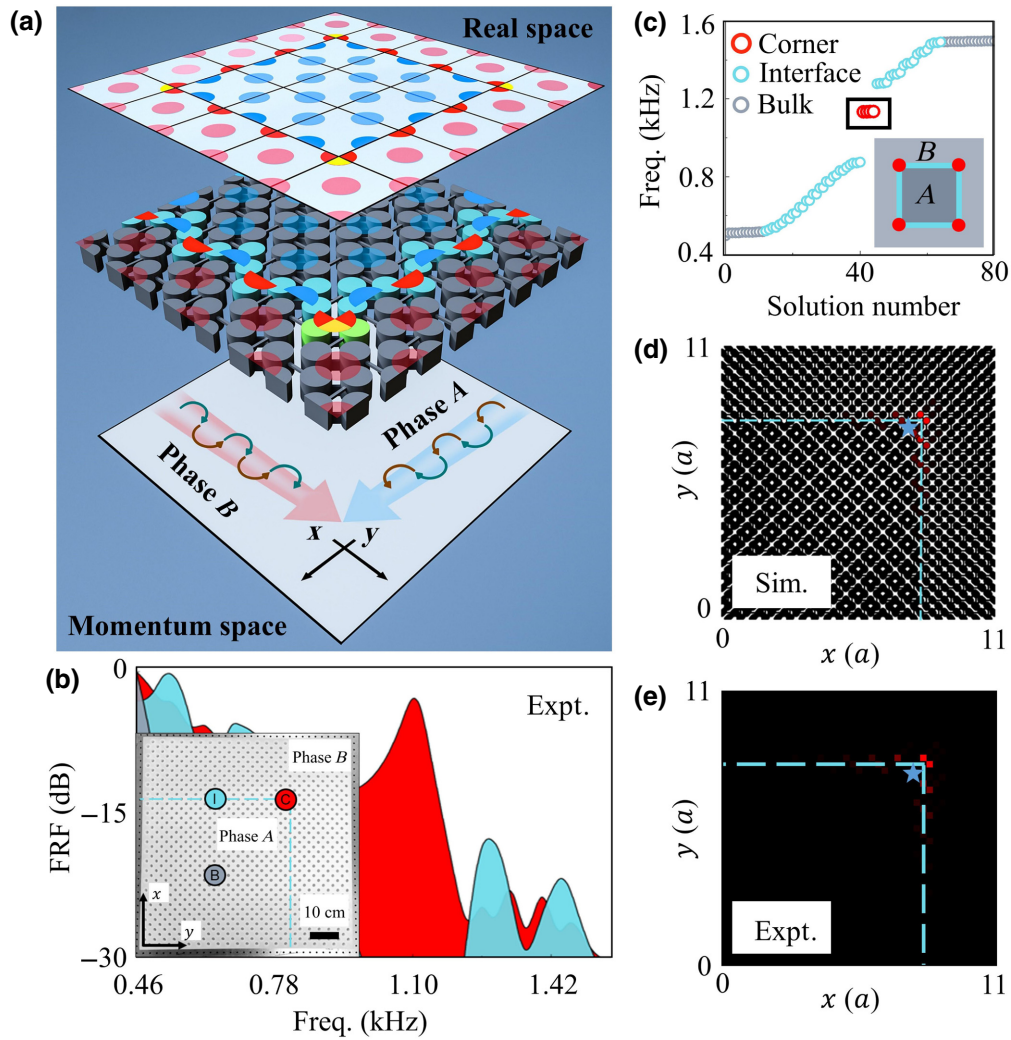


FIG. 4. Topological corner states in the combined system. (a) Schematic Wannier configurations for corner states. The real-space Wannier configurations (upper panel) are attached to corresponding PCs (middle panel), manifesting charge anomaly at the corner sites (green cavities). Lower panel illustrates gapped interface states of  $+k_x$  and  $+k_y$  with specific PPs. (b) Measured FRFs for the corner, edge, and bulk states colored in red, blue, and gray, respectively. Inset is a photograph of the sample containing one corner, where the corner (C), interface (I), and bulk (B) probes are labeled. (c) Simulated eigenstate spectrum for the  $C_4$ -symmetric PCs. (d),(e) Simulated and measured acoustic pressure fields at 1.1 kHz. The blue dashed lines denote the interfaces.

The curl of Poynting vectors denotes the value of acoustic local angular momentum, representing the nonzero pseudospin feature of the interface states [40,41]. In Fig. 2(d), we simulate the PP distributions for two wave vectors with inverse directions, i.e.,  $k_y = 0.8 \pi/a$  and  $1.2 \pi/a$ . The PPs predominantly localize at the unit cells right beside the interface as expected ( $n_x = 10, 11$ ). Specifically, for  $k_y = 0.8$  (red dotted line), the PP is negative for  $n_x = 10$  and positive for  $n_x = 11$ , while for  $k_y = 1.2$  (green dotted line) the PP manifests opposite distributions. This locking feature is illustrated in the lower panel of Fig. 2(a), revealing that the proposed topological interface states are helical.

The serpentine propagation of the interface states can be observed by detecting acoustic fields under the

point-source excitation on the interface. At the frequency of 1.4 kHz, simulated and measured acoustic field profiles are presented in Figs. 3(a) and 3(b), respectively. The simulations and measurements together show that acoustic waves are well localized and propagate in a serpentine path along the interface between phases A and B. More importantly, the PP properties of the interface states can be directly observed. For the interface states at 0.6 kHz, we simulate the  $z$  components of the curl of the Poynting vector,  $(\nabla \times \mathcal{S}_{\text{ave}})_z$ , in the same PC with  $6 \times 20$  unit cells. The simulated results are in the middle panel of Fig. 3(c). In experiment, we measure  $\mathcal{S}_{\text{ave}}$  in four cavities near the source by acoustic velocity detection, and show their distributions by normalized arrows in the four insets of Fig. 3(c) (see Appendix A for details). For the interface state

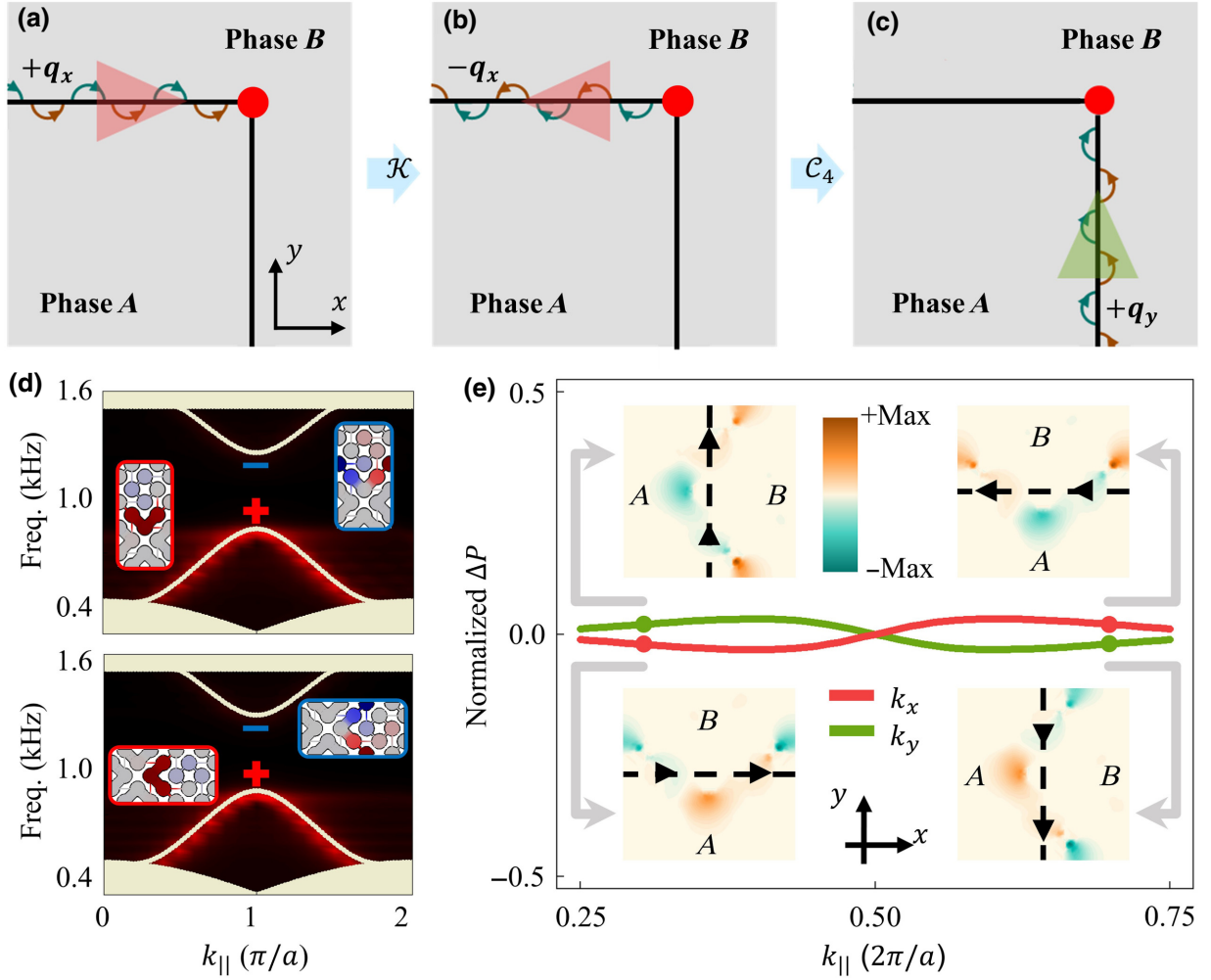


FIG. 5. (a)–(c) Illustration for the operator  $\mathcal{C}_4\mathcal{K}$  connecting  $x$  and  $y$  interfaces. The large arrows colored in red and green denote the acoustic waves travelling along  $x$  and  $y$  directions, respectively. The small arrows represent the PP properties carried by the acoustic waves. (d) Simulated (lines) and measured (color maps) projected dispersions of gapped interface states along the  $x$  (upper panel) and  $y$  (lower panel) directions. Insets show acoustic pressure field distributions for  $k_x/k_y = \pi/a$ . Red and blue symbols denote the symmetries of the interface states. (e) PP distributions of the interface states along  $x$  (red) and  $y$  (green) directions. Insets show simulated PP profiles of the eigenstates for  $k_{||} = 0.3$  and  $k_{||} = 0.7$  in units of  $2\pi/a$ .

travelling along the  $+y$  direction, the measured  $\mathcal{S}_{\text{ave}}$  reveals clockwise Poynting vector distributions in phase  $A$  (upper left inset) and anticlockwise ones in phase  $B$  (upper right inset). The curl profiles are in compliance with the simulations and capture the acoustic pseudospin textures well. The measured results hold opposite distributions for the interface state along the  $-y$  direction, providing strong evidence for the PP-momentum locking feature. Moreover, for the interface state along a particular direction, the PPs with opposite chirality are interleaved at the domain wall of the two phases, showing that both of the two phases are essential for the propagation of the snaking interface states. The corresponding Hamiltonian analysis in the perspective of pseudospin is provided in Sec. 5 of Ref. [49].

#### IV. CORNER STATES REVEALING TOPOLOGICAL CHARGE ANOMALY

We embed the PC of phase  $A$  into that of phase  $B$  to explore higher-order topology in a combined PC illustrated in the middle panel of Fig. 4(a). For the emergence of corner states, the interface states are gapped by breaking the glide symmetries, which is realized by enlarging the nearest hopping tubes in the PC of phase  $A$  and shrinking those in the PC of phase  $B$  [49]. From the simulated eigenstate spectrum in Fig. 4(c), we conclude that such combined PCs host gapped interface states with visible gaps ranging from 0.88 to 1.26 kHz, and the corner states (red dots) emerge in the interface band gap and are nearly degenerate at 1.12 kHz. Topological properties of the corner states in

the combined PC can be uncovered by analyzing the corresponding Wannier configuration exhibited in the upper panel of Fig. 4(a). The SWFs for the gapped interface states carry trivial interface charges and make no contribution to the corner states. In contrast, the corner orbital contains three SWFs corresponding to the EBRs  $(A)_{1b}$ , of which one orbital is from the outer bulk PCs (yellow quadrants) and the other two are from the converged interfaces (red quadrants). They each host  $1/4$  charge and the total charge is pictorially read as  $1/4 \times 3 = 3/4$  (Sec. 6, Ref. [49]). Such mismatch between local corner charges and the fourfold rotation symmetry is regarded as the fractional corner anomaly [20,21], leading to the proposed  $C_4$ -symmetric corner states.

In experiments, we construct a sample containing one corner between two PCs of phases  $A$  and  $B$  where the bulk, interface, and corner states coexist (see Ref. [49] for the sample photo). The simulated [Fig. 4(d)] and measured [Fig. 4(e)] acoustic pressure distributions together illustrate the well-localized corner states. The measured FRFs for the bulk, interface, and corner states are in Fig. 4(b) where the corner state emerges as a sharp red peak at 1.1 kHz. The blue regions representing interface states extend in two frequency ranges, which are from 0.52 to 0.92 kHz and from 1.3 to 1.55 kHz.

Moreover, we offer the projected dispersions along the  $x$  and  $y$  directions in the upper and lower panels of Fig. 5(d), respectively. Different from the previous work where the corner mode is caused by two adjacent interfaces with different dipole moments [34], the  $C_4$  rotation symmetry ensures that the two interfaces host identical dispersions, and the eigenstates at the Brillouin zone boundaries have the same symmetry labels. For both the interface states along the  $x$  and  $y$  directions, the insets of Fig. 5(d) indicate that the parity of the acoustic field is even for the lower band and odd for the higher band. Such symmetry signatures indicate trivial interface dipole moments, giving rise to the well-defined corner states with  $C_4$  symmetry [20].

Although the  $C_4$  symmetry guarantees the uniform acoustic pressure distributions on the interface, we notice that the gapped interface states along the  $+x$  and  $+y$  directions host reverse PP profiles, which follows from the fact that they are related by the symmetry operator  $C_4\mathcal{K}$ . As illustrated in Figs. 5(a)–5(c), when the time-reversal operator  $\mathcal{K}$  acts on the interface state along the  $x$  direction, the wave vector  $q_x$  [Fig. 5(a)] is changed into  $-q_x$  [Fig. 5(b)] with the corresponding PPs reversed. The wave vector  $-q_x$  is then changed into  $+q_y$  [Fig. 5(c)] by the operator  $C_4$  with the PPs unchanged. A consistent Hamiltonian analysis is in Sec. 7, Ref. [49]. To confirm these depictions, we numerically calculate  $\Delta P$ , which is defined as the difference between the PP in phase  $B$  and that in phase  $A$ . In Fig. 5(e), we provide the results of the gapped interface states travelling along the  $x$  (red) and  $y$  (green) directions. With the wave vectors  $k_x$  and  $k_y$  fixed at  $0.6 \pi/a$ ,  $\Delta P$  is positive in

phase  $A$  and negative in phase  $B$  when the interface states travel along the  $+x$  direction (lower left inset), whereas the sign of  $\Delta P$  is inverse for the wave along  $+y$  (upper left inset). Similar analysis also applies to other wave vectors, e.g.,  $k_{\parallel} = 1.4 \pi/a$  (two right insets). In all, the gapped interface states along the  $x$  and  $y$  directions manifest opposite PP spectra. The proposed PP-induced spectrum inversion is expected to provide alternative degrees of freedom in angular momentum manipulations.

## V. CONCLUSION AND OUTLOOKS

In conclusion, we provide a tractable procedure to design topological PCs from the perspective of Wannier configurations in real space. The proposed PCs are further utilized to observe multidimensional crystalline topology, where the obtained interface states are protected by the spatial mismatch of real-space Wannier configurations, and the corner states are due to the quantized corner charge anomaly. Experimentally, we measure the PP profiles of the first-order interface states to depict the topological transport properties. Our findings with the multidimensional interface modes are applied in a more general system without quadrupole moments [36] to facilitate understanding the real- and momentum-space duality in acoustic topological systems. The proposed paradigm does not just apply in group  $p4$ , but can be implemented for other space group symmetries. The observed multidimensional interface transports also have potential applications for acoustic functional devices and broadband wave control, and can be implemented in other classical wave systems.

## ACKNOWLEDGMENT

This work is supported by the Key-Area Research and Development Program of Guangdong Province (Grant No. 2020B010190002), the National Natural Science Foundation of China (Grants No. 11890701, No. 11874483, No. 12104480, No. 11974005), and the IACAS Frontier Exploration Project (Grant No. QYTS202110).

## APPENDIX A: METHODS FOR EXPERIMENTS AND NUMERICAL SIMULATIONS

Our samples are made with acrylic-based light-activated resin by three-dimensional (3D) printing. Considering the huge acoustic impedance mismatch between air and resin, the 3D-printed materials with sufficient thickness can be regarded as rigid boundaries. Circular channels are intentionally introduced on the top side of each cavity for exciting and measuring the acoustic waves. When not in use, these channels are blocked by rubber plugs.

The measured projected bands of the interface states are obtained by Fourier transforming the scanned acoustic

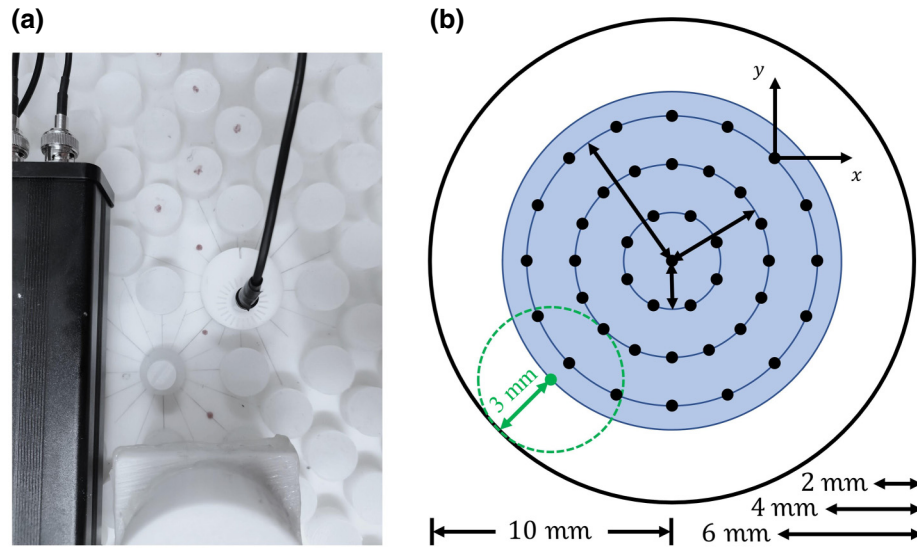


FIG. 6. Experimental settings of acoustic Poynting vectors. (a) Experimental devices for measuring acoustic Poynting vectors. (b) Measurement points in one acoustic cavity. The green dashed circle represents the cross section of the acoustic particle velocity sensor.

pressure fields. The sound is generated by a loudspeaker and then guided into the channels of the samples from the channels mentioned previously. A 1/4-in. microphone (Brüel & Kjær Type-4939) is used to detect acoustic signals from these channels. We scan our samples to obtain the acoustic pressure field distribution, which is expressed as site-resolved response functions. Then the measured projection bands in momentum space are obtained by Fourier transformation.

The measured results of acoustic FRFs for bulk, edge, and corner states are obtained by acoustic near-field pump-probe detection. The source, as pumps, is placed in the center of the bulk, at the interface between phase *A* and phase *B*, and in turn close to the intersection of the two converging interfaces. The measuring microphone is mounted in the cavity near the pumping cavity. The cavities for pumps and probes are not connected by coupling tubes to eliminate the local resonance. All measured signals are collected and analyzed using a multianalyzer system (Brüel & Kjær Type-3160).

The experimental results of acoustic Poynting vectors in Fig. 3(c) are measured by a 1/4-in. acoustic particle velocity sensor and the supporting signal acquisition system (Nanjing Particle Acoustics Technology Co. Ltd.). We measure the *x*-direction and *y*-direction components of the acoustic Poynting vectors at a fixed point in the cavity, and then orthogonally synthesize them to obtain the results. By placing the probe at different radii of the cavity and rotating the probe evenly in the angular direction, we achieve full coverage of detection points in the whole cavity and obtain the acoustic Poynting vector distributions. The results are formed by taking the measurement results of 41 points with radii 0, 2, 4, and 6 mm. The arrows with normalized length show the directions of  $\mathcal{S}_{\text{ave}}$ .

We present the acoustic particle velocity vector sensor in Fig. 6(a), and illustrate how to divide the cavities with the probe points in Fig. 6(b). Since the radius of the acoustic particle vector sensor (the green dashed circle) is 3 mm, the maximum area available for measurement is shown as a blue circle with the radius 7 mm. Three smaller circles with radii 2, 4, and 6 mm are chosen for the measurements. Sixteen probe points are distributed evenly on the two outmost circles while eight probe points are on the inner circle. Together with the center-point, there are 41 measurement points in each cavity.

The numerical simulations in this work are performed with the 3D acoustic pressure module of the commercial finite-element simulation software COMSOL Multiphysics. The density and sound velocity of air are taken as  $1.21 \text{ kg/m}^3$  and  $343 \text{ m/s}$ , respectively. To calculate the band structures in Figs. 1(e) and 1(f), all four outmost boundaries of the unit cell are set as Floquet-Bloch periodic boundaries. For projected dispersions, the boundaries of the ribbon supercells are set as the Floquet-Bloch periodic condition along the interface direction, and the others are set as the plane-wave radiation condition. The sample boundaries for corner states are set as the plane-wave radiation condition when calculating the eigenstate spectra.

## APPENDIX B: CALCULATIONS OF THE REAL-SPACE TOPOLOGICAL INDICATORS

The genuine topological invariants for wallpaper group  $p4$  can be obtained by inspecting the corresponding relationship between real and momentum space. With the correspondence between the real-space Wannier orbitals and the symmetry labels at high-symmetry points (HSP) in momentum space, a set of linear equations Eq. (B1) can



be derived,

$$\begin{aligned}
 v_{1a,1} &= -3\Gamma_1 - \frac{3}{2}\Gamma_i - \Gamma_{-1} - \frac{3}{2}\Gamma_{-i} + \frac{3}{2}M_i + 2M_{-1}, \\
 &\quad + \frac{3}{2}M_{-i} + X_{-1}, \\
 v_{1a,i} &= \Gamma_1 - \frac{1}{2}\Gamma_i + \Gamma_{-1} + \frac{3}{2}\Gamma_{-i} - \frac{3}{2}M_i + \frac{1}{2}M_{-i} - X_{-1}, \\
 v_{1a,-1} &= \Gamma_1 + \frac{1}{2}\Gamma_i - \Gamma_{-1} + \frac{1}{2}\Gamma_{-i} \\
 &\quad - \frac{1}{2}M_i - 2M_{-1} - \frac{1}{2}M_{-i} + X_{-1}, \\
 v_{1b,1} &= \frac{3}{2}\Gamma_i + 2\Gamma_{-1} + \frac{3}{2}\Gamma_{-i} \\
 &\quad - \frac{1}{2}M_i - 2M_{-1} - \frac{1}{2}M_{-i} - X_{-1}, \\
 v_{1b,i} &= -\frac{3}{2}\Gamma_i + \frac{1}{2}\Gamma_{-i} \\
 &\quad + \frac{1}{2}M_i - \frac{3}{2}M_{-i} + X_{-1}, \\
 v_{1b,-1} &= -\frac{1}{2}\Gamma_i - 2\Gamma_{-1} - \frac{1}{2}\Gamma_{-i} \\
 &\quad + \frac{3}{2}M_i + 2M_{-1} + \frac{3}{2}M_{-i} - X_{-1}, \\
 v_{2c} &= \frac{1}{2}\Gamma_i + \frac{1}{2}\Gamma_{-i} - \frac{1}{2}M_i - \frac{1}{2}M_{-i}. \tag{B1}
 \end{aligned}$$

We then obtain the integer topological indicators  $v_{W,\lambda}$  for each EBR by calculating Eq. (B1) and all calculation results are tabulated in Table S2 in the Supplemental Material [49]. We take the first row as an example to elaborate the calculated results. Only the values of  $v_{1a,\pm 1}$  and  $v_{1a,\pm i}$  are nonzero since the SWF is centered at the WP  $1a$ .  $v_{1a,1} = -3$  corresponds to  $\lambda = 1$ , indicating that the SWF centered at  $1a$  hosts an  $s$  orbital. In addition, time-reversal symmetry is always preserved in our PCs, which can be reflected by the fact that  $v_{1a,1} + v_{1a,-1} + v_{1a,i} + v_{1a,-i} = 0$ . Here we list all ten integers even though some of them can be reduced. Since only the  $s$  mode survives at  $\Gamma$  for the lowest-frequency band in the classical acoustic system, the first two bands support three EBRs:  $(A)_{1a}$ ,  $(A)_{1b}$ , and  $(A)_{2c}$ , which are shown in bold in Table I. By checking Table I, we find that the decomposed acoustic modes at the HSPs are consistent with  $(A)_{1a}$  and  $(A)_{1b}$  for phase  $A$ , and the acoustic modes are consistent with  $(A)_{2c}$  for phase  $B$ . We reduce the proposed RSTIs as a set of three corresponding topological indicators  $(v_{1a,1} \ v_{1b,1} \ v_{2c,1})$ . The RSTIs of phase  $A$  and phase  $B$  thus read  $(-3, -3, 0)$  and  $(0, 0, -1)$ , respectively. In fact, the same  $v_{W,\lambda}$  can be obtained from the real-space Wannier configuration [19] as well. Such consistency proves the duality between the real and momentum space.

TABLE I. Correspondence between the Wannier functions in real space and the symmetry labels in momentum space and the calculated RSTIs.  $W, \lambda$ , and  $\rho$  denote WPs, rotation eigenvalues, and EBRs, respectively.  $v_{W,\lambda}$  is the symmetry indicator of the RSTIs.  $\Gamma_\lambda$  is the multiplicity of the rotation eigenvalues at HSPs in momentum space.

Real space		Momentum space																				
$W$	$\lambda$	$\rho$	$v_{1a,1}$	$v_{1a,-1}$	$v_{1a,i}$	$v_{1a,-i}$	$v_{1b,1}$	$v_{1b,-1}$	$v_{1b,i}$	$v_{1b,-i}$	$v_{2c,1}$	$v_{2c,-1}$	$\Gamma_1$	$\Gamma_{-1}$	$\Gamma_i$	$\Gamma_{-i}$	$M_1$	$M_{-1}$	$M_i$	$M_{-i}$	$X_1$	$X_{-1}$
<b>1a</b>	1	<b><math>(A)_{1a}</math></b>	<b>-3</b>	1	1	1	0	0	0	0	0	0	1	0	0	0	0	1	0	0	1	0
	-1	<b><math>(B)_{1a}</math></b>	1	-3	1	-3	0	0	0	0	0	0	0	1	0	1	0	0	0	0	0	0
	$i$	$(^1E^2E)_{1a}$	1	1	1	1	0	0	0	0	0	0	0	0	0	0	0	0	1	0	0	0
<b>1b</b>	-i	$(^1E^2E)_{1a}$	1	1	1	1	0	0	0	0	0	0	0	0	0	0	0	0	0	0	0	0
	1	<b><math>(A)_{1b}</math></b>	0	0	0	0	1	1	1	1	0	0	0	0	0	0	0	1	0	0	0	0
	-1	<b><math>(B)_{1b}</math></b>	0	0	0	0	1	1	1	1	0	0	0	0	0	0	0	0	0	0	0	0
<b>2c</b>	-i	$(^1E^2E)_{1b}$	0	0	0	0	1	1	1	1	0	0	0	0	0	0	0	0	0	0	0	0
	1	<b><math>(A)_{2c}</math></b>	0	0	0	0	1	1	1	1	0	0	0	0	0	0	0	0	0	0	0	0
	-1	<b><math>(B)_{2c}</math></b>	0	0	0	0	1	1	1	1	-1	-1	0	0	0	0	0	0	0	0	0	0

### APPENDIX C: GAPLESS INTERFACE STATES INDUCED BY WANNIER CONFIGURATIONS

We provide schematic Wannier configurations in Fig. 7(a) for phase *A* and in Fig. 7(c) for phase *B*. These illustrations of the projected position operators of the SWFs correspond to the Wilson loop spectra [5] of the two lowest energy bands. With  $k_y$  running from 0 to  $2\pi$  in the BZ for phase *A* [Fig. 7(b)] and phase *B* [Fig. 7(d)], we obtain the  $k_y$ -dependent Wannier centers  $v_{x,A}^j$  and  $v_{x,B}^j$  by extracting eigenstates from the tight-binding model ( $j = 1, 2$  for the band index). For both phase *A* and phase *B*,  $(v_x^1, v_x^2)$  is  $(0, 0.5)$ . The calculated  $v_x^j$  explicitly shows that the dipole moments  $p_{x,A}$  and  $p_{x,B}$  of the two phases, i.e., the sum sectors of  $v_x^j$  for the two lowest-frequency bands, read  $p_{x,A} = p_{x,B} = 1/2 \bmod 1$ . Similar analyses apply to the  $x$

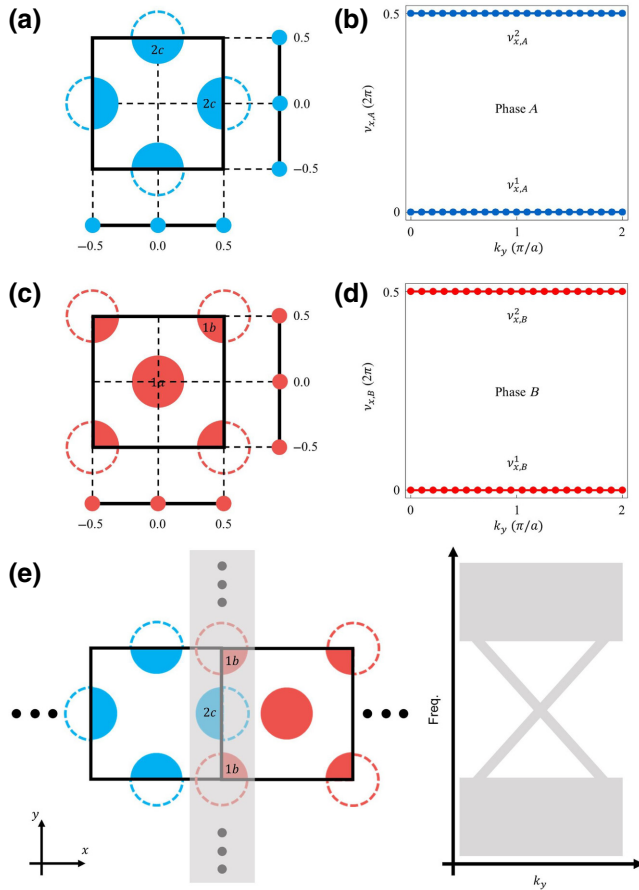


FIG. 7. Schematics of the SWFs and Wilson loop spectra for phases *A* and *B*. (a)  $2c$ -centered SWFs with local charges in phase *A*. The projected localized positions of the SWFs are also given. (b) Calculated  $k_y$ -dependent Wannier bands of the first two energy bands for phase *A*. (c), (d)  $1a$ -centered and  $1b$ -centered SWFs with local charges and the Wannier bands of phase *B*. (e) Illustrations for combining the Wannier configurations of phases *A* and *B* (left panel), giving rise to the gapless interface states (right panel).

direction owing to the  $C_4$  rotation symmetry. The calculated results are consistent with the schematic localized Wannier functions.

The calculated results for phase *A* [Fig. 7(b)] and for phase *B* [Fig. 7(d)] seem to be identical, showing that the hybrid Wannier center for one band is 0 and for the other band is  $\pi$ . However, can we thus affirm that these two phases are the same? The answer is no. From the schematic Wannier configurations in Fig. 7(a), we can read that the SWFs all center at the WP  $2c$  in phase *A*. When these SWFs are projected onto the  $x$  axis, their Wannier centers, illustrated in Fig. 7(a) as blue dots, are at the center and the boundary of the projected lattice and correspond to the calculation results 0 and  $\pi$  in Fig. 7(b). However, in Fig. 7(c), the SWFs centered at the WPs  $1a$  and  $1b$  (phase *B*) can also lead to same Wilson loop spectra. Above analyses are also suitable for the  $y$  direction owing to the  $C_4$  rotation symmetry. Henceforth, the topological properties of phases *A* and *B* cannot be distinguished without the proposed Wannier configuration approaches.

This discussion of the Wilson loop spectra indicates possible gapped boundary states when phase *A* or phase *B* exist separately. However, we can construct gapless interface states by inspecting the boundary signatures of Wannier configurations as illustrated Fig. 7(e). By combining phases *A* and *B* together, the associated SWFs can center at both the WP  $1b$  and  $2c$  (left panel). The proposed gapless interface states (right panel) are thus regarded as the Wannier center flows on the interface as discussed in the main text.

- [1] M. Z. Hasan and C. L. Kane, Colloquium: Topological insulators, *Rev. Mod. Phys.* **82**, 3045 (2010).
- [2] X. Qi and S. Zhang, Topological insulators and superconductors, *Rev. Mod. Phys.* **83**, 1057 (2011).
- [3] Y. Hatsugai, Chern Number and Edge States in the Integer Quantum Hall Effect, *Phys. Rev. Lett.* **71**, 3697 (1993).
- [4] C. K. Chiu, J. C. Y. Teo, A. P. Schnyder, and S. Ryu, Classification of topological quantum matter with symmetries, *Rev. Mod. Phys.* **88**, 035005 (2016).
- [5] R. Yu, X. L. Qi, B. A. Bernevig, Z. Fang, and X. Dai, Equivalent expression of  $Z_2$  topological invariant for band insulators using the non-Abelian Berry connection, *Phys. Rev. B* **84**, 075119 (2011).
- [6] M. Di Liberto, N. Goldman, and G. Palumbo, Non-Abelian Bloch oscillations in higher-order topological insulators, *Nat. Commun.* **11**, 5942 (2020).
- [7] L. Fu, Topological Crystalline Insulators, *Phys. Rev. Lett.* **106**, 106802 (2011).
- [8] Y. Ando and L. Fu, Topological crystalline insulators and topological superconductors: from concepts to Materials, *Annu. Rev. Condens. Matter Phys.* **6**, 361 (2015).
- [9] B. Bradlyn, L. Elcoro, J. Cano, M. G. Vergniory, Z. Wang, C. Felser, M. I. Aroyo, and B. A. Bernevig, Topological quantum chemistry, *Nature* **547**, 298 (2017).

- [10] H. C. Po, A. Vishwanath, and H. Watanabe, Symmetry-based indicators of band topology in the 230 space groups, *Nat. Commun.* **8**, 50 (2017).
- [11] J. Kruthoff, J. de Boer, J. van Wezel, C. L. Kane, and R. J. Slager, Topological Classification of Crystalline Insulators through Band Structure Combinatorics, *Phys. Rev. X* **7**, 041096 (2017).
- [12] L. Elcoro, B. Bradlyn, Z. Wang, M. G. Vergniory, J. Cano, C. Felser, B. A. Bernevig, D. Orobengoa, G. de la Flor and M. I. Aroyo, Double crystallographic groups and their representations on the Bilbao Crystallographic Server, *J. Appl. Cryst.* **50**, 1457 (2017).
- [13] D. Vanderbilt and R. D. King-Smith, Electric polarization as a bulk quantity and its relation to surface charge, *Phys. Rev. B* **48**, 4442 (1993).
- [14] N. Marzari, A. A. Mostofi, J. R. Yates, I. Souza, and D. Vanderbilt, Maximally localized Wannier functions: Theory and applications, *Rev. Mod. Phys.* **84**, 1419 (2012).
- [15] W. A. Benalcazar, B. A. Bernevig, and T. L. Hughes, Quantized electric multipole insulators, *Science* **357**, 61 (2017).
- [16] W. A. Benalcazar, B. A. Bernevig, and T. L. Hughes, Electric multipole moments, topological multipole moment pumping, and chiral hinge states in crystalline insulators, *Phys. Rev. B* **96**, 245115 (2017).
- [17] Z. Song, Z. Fang, and C. Fang, (d-2)-Dimensional Edge States of Rotation Symmetry Protected Topological States, *Phys. Rev. Lett.* **119**, 246402 (2017).
- [18] F. Schindler, A. M. Cook, M. G. Vergniory, Z. Wang, S. S. P. Parkin, B. A. Bernevig, and T. Neupert, Higher-order topological insulators, *Sci. Adv.* **4**, eaat0346 (2018).
- [19] G. van Miert and C. Ortix, Higher-order topological insulators protected by inversion and rotoinversion symmetries, *Phys. Rev. B* **98**, 081110 (2018).
- [20] W. A. Benalcazar, T. Li, and T. L. Hughes, Quantization of fractional corner charge in  $C_n$ -symmetric higher-order topological crystalline insulators, *Phys. Rev. B* **99**, 245151 (2019).
- [21] C. W. Peterson, T. Li, W. A. Benalcazar, T. L. Hughes, and G. Bahl, A fractional corner anomaly reveals higher-order topology, *Science* **368**, 1114 (2020).
- [22] Z. D. Song, L. Elcoro, and B. A. Bernevig, Twisted bulk-boundary correspondence of fragile topology, *Science* **367**, 794 (2020).
- [23] V. Peri, Z. D. Song, M. Serra-Garcia, P. Engeler, R. Queiroz, X. Huang, W. Deng, Z. Liu, B. A. Bernevig, and S. D. Huber, Experimental characterization of fragile topology in an acoustic metamaterial, *Science* **367**, 797 (2020).
- [24] Y. Liu, S. Leung, F. F. Li, Z. K. Lin, X. Tao, Y. Poo, and J. H. Jiang, Bulk-disclination correspondence in topological crystalline insulators, *Nature* **589**, 381 (2021).
- [25] A. B. Khanikaev, R. Fleury, S. H. Mousavi, and A. Alu, Topologically robust sound propagation in an angular-momentum-biased graphene-like resonator lattice, *Nat. Commun.* **6**, 8260 (2015).
- [26] C. He, X. Ni, H. Ge, X. C. Sun, Y. B. Chen, M. H. Lu, X. P. Liu, and Y. F. Chen, Acoustic topological insulator and robust one-way sound transport, *Nat. Phys.* **12**, 1124 (2016).
- [27] J. Lu, C. Qiu, L. Ye, X. Fan, M. Ke, F. Zhang, and Z. Liu, Observation of topological valley transport of sound in sonic crystals, *Nat. Phys.* **13**, 369 (2016).
- [28] Y. G. Peng, C. Z. Qin, D. G. Zhao, Y. X. Shen, X. Y. Xu, M. Bao, H. Jia, and X. F. Zhu, Experimental demonstration of anomalous Floquet topological insulator for sound, *Nat. Commun.* **7**, 13368 (2016).
- [29] Y. Ding, Y. Peng, Y. Zhu, X. Fan, J. Yang, B. Liang, X. Zhu, X. Wan, and J. Cheng, Experimental Demonstration of Acoustic Chern Insulators, *Phys. Rev. Lett.* **122**, 014402 (2019).
- [30] B. Hu, Z. Zhang, H. Zhang, L. Zheng, W. Xiong, Z. Yue, X. Wang, J. Xu, Y. Cheng, X. Liu, and J. Christensen, Non-Hermitian topological whispering gallery, *Nature* **597**, 655 (2021).
- [31] M. Serra-Garcia, V. Peri, R. Susstrunk, O. R. Bilal, T. Larsen, L. G. Villanueva, and S. D. Huber, Observation of a phononic quadrupole topological insulator, *Nature* **555**, 342 (2018).
- [32] X. Ni, M. Weiner, A. Alu, and A. B. Khanikaev, Observation of higher-order topological acoustic states protected by generalized chiral symmetry, *Nat. Mater.* **18**, 113 (2019).
- [33] H. Xue, Y. Yang, F. Gao, Y. Chong, and B. Zhang, Acoustic higher-order topological insulator on a kagome lattice, *Nat. Mater.* **18**, 108 (2019).
- [34] X. J. Zhang, H. X. Wang, Z. K. Lin, Y. Tian, B. Xie, M. H. Lu, Y. F. Chen, and J. H. Jiang, Second-order topology and multidimensional topological transitions in sonic crystals, *Nat. Phys.* **15**, 582 (2019).
- [35] Y. Qi, C. Qiu, M. Xiao, H. He, M. Kea, and Z. Liu, Acoustic Realization of Quadrupole Topological Insulators, *Phys. Rev. Lett.* **124**, 206601 (2020).
- [36] X. Zhang, Z. K. Lin, H. X. Wang, Z. Xiong, Y. Tian, M. H. Lu, Y. F. Chen, and J. H. Jiang, Symmetry-protected hierarchy of anomalous multipole topological band gaps in nonsymmorphic metacrystals, *Nat. Commun.* **11**, 65 (2020).
- [37] Q. Guo, T. Jiang, R. Y. Zhang, L. Zhang, Z. Q. Zhang, B. Yang, S. Zhang, and C. T. Chan, Experimental observation of non-Abelian topological charges and edge states, *Nature* **594**, 195 (2021).
- [38] B. Jiang, A. Bouhon, Z. K. Lin, X. X. Zhou, B. Hou, F. Li, R. J. Slager, and J. H. Jiang, Experimental observation of non-Abelian topological acoustic semimetals and their phase transitions, *Nat. Phys.* **17**, 1239 (2021).
- [39] Z. Lin, Y. Wu, B. Jiang, Y. Liu, S. Wu, F. Li, and J. H. Jiang, Topological Wannier cycles induced by sub-unit-cell artificial gauge flux in a sonic crystal, *Nat. Mater.* **21**, 430 (2022).
- [40] L. Zhang and Q. Niu, Angular Momentum of Phonons and the Einstein-de Haas Effect, *Phys. Rev. Lett.* **112**, 085503 (2014).
- [41] L. Zhang and Q. Niu, Chiral Phonons at High-Symmetry Points in Monolayer Hexagonal Lattices, *Phys. Rev. Lett.* **115**, 115502 (2015).
- [42] Y. Long, J. Ren, and H. Chen, Intrinsic spin of elastic waves, *Proc. Natl. Acad. Sci. U. S. A.* **115**, 9951 (2018).
- [43] C. Shi, R. Zhao, Y. Long, S. Yang, Y. Wang, H. Chen, J. Ren, and X. Zhang, Observation of acoustic spin, *Natl. Sci. Rev.* **6**, 707 (2019).

- [44] Y. Long, D. Zhang, C. Yang, J. Ge, H. Chen, and J. Ren, Realization of acoustic spin transport in metasurface waveguides, *Nat. Commun.* **11**, 4716 (2020).
- [45] Y. Long, H. Ge, D. Zhang, X. Xu, J. Ren, M. H. Lu, M. Bao, H. Chen, and Y. F. Chen, Symmetry selective directionality in near-field acoustics, *Natl. Sci. Rev.* **7**, 1024 (2020).
- [46] H. Ge, X. Y. Xu, L. Liu, R. Xu, Z. K. Lin, S. Y. Yu, M. Bao, J. H. Jiang, M. H. Lu, and Y. F. Chen, Observation of Acoustic Skyrmions, *Phys. Rev. Lett.* **127**, 144502 (2021).
- [47] S. Wang, G. Zhang, X. Wang, Q. Tong, J. Li, and G. Ma, Spin-orbit interactions of transverse sound, *Nat. Commun.* **12**, 6125 (2021).
- [48] H. Yang and S. Lee, Topological phases of nonsymmorphic crystals: Shastry-Sutherland lattice at integer filling, *Phys. Rev. B* **99**, 165140 (2019).
- [49] See Supplemental Material at <http://link.aps.org/supplemental/10.1103/PhysRevApplied.18.064094> for discussions about sample fabrication, measurement techniques, and the relevant theoretical analyses and experimental demonstrations.